Cation-site Disordered Cu_3PdN Nanoparticles for Hydrogen Evolution Electrocatalysis

Sani Y. Harouna-Mayer[#], Jagadesh Kopula Kesavan[#], Francesco Caddeo[#], Lian Belgardt, Chia-Shuo Hsu, Lars Klemeyer, Lizzi Kipping, Melike Gumus Akcaalan, Tjark R.L. Groene, Andrea Koeppen, Olivier Mathon, Ann-Christin Dippel, Dorota Koziej**

[#]S.Y. Harouna-Mayer, J. Kopula Kesavan and F. Caddeo contributed equally.

S.Y. Harouna-Mayer, J. Kopula Kesavan, F. Caddeo, L. Belgardt, C. Hsu, L. Klemeyer, M. Gumus Akcaalan, T.R.L. Groene, D. Koziej
University of Hamburg, Institute for Nanostructure and Solid-State Physics, Center for Hybrid Nanostructures (CHyN), 22761 Hamburg Germany
E-mail: dorota.koziej@uni-hamburg.de

S.Y. Harouna-Mayer, J. Kopula Kesavan, D. Koziej
The Hamburg Center for Ultrafast Imaging, 22761 Hamburg Germany

A. Koeppen
University of Hamburg, Department of Chemistry, 20146 Hamburg, Germany

O. Mathon
European Synchrotron Radiation Facility (ESRF), 38043 Grenoble, France

A. Dippel
Deutsches Elektronen-Synchrotron DESY, 22607 Hamburg, Germany

Keywords: cation disorder, ternary metal nitrides, anti-perovskite structure, double-edge EXAFS refinement, in situ X-ray absorption and scattering studies, hydrogen evolution reaction

Transition metal nitrides (TMNs) are emerging as a promising class of materials for application in optoelectronics as well as energy conversion and storage, but they remain rather unexplored, mainly due to a lack of mechanistic understanding of their synthetic pathways. Here we demonstrate a one-pot synthesis, which yields 3 nm phase-pure Cu_3PdN nanoparticles after the reaction of Cu methoxide and Pd acetylacetonate in benzylamine for 5 minutes at 140 °C. We reveal the structure of the initial complexes and their conversion to Cu_3PdN by in situ x-ray absorption spectroscopy measurements and elucidate nucleation and growth of the nitride nanocrystals by in situ total x-ray scattering measurements. Interestingly, extended x-ray absorption fine structure double-edge refinement reveals the presence of short-range cation-site disorder in the anti-perovskite structure of Cu_3PdN, which has not been observed before in the Cu_3PdN system. Additionally, the synthesized Cu_3PdN nanoparticles are tested for the electrocatalytic hydrogen evolution reaction revealing an overpotential as low as η_{10} = 212 ± 11 mV measured at 10 mA/cm^2.

1. Introduction

Transition metal nitrides (TMNs) are a versatile class of materials that exhibit properties of covalent compounds, ionic crystals and transition metals.[1–3] The incorporation of the nitride (N^{3-}) anion into the metal sublattice causes expansion of the parent metal lattice and metal d-band broadening.[4–6] These unique electronic and bonding characteristics give rise to numerous applications particularly in energy conversion and storage.[2,3,7–9] Recent studies explored several TMNs as materials of interest for electrochemical energy conversion, focusing on the influence of morphology[10–12], defect engineering[13–15], heteroatom doping[16,17], heterostructuring[18,19] or alloying[20,21] on their electrochemical performance. Despite the progress, challenges remain, such as achieving scalability, stability in aqueous media or cost-effective and green synthetic methods, since TMN synthesis typically involves steps at high temperatures and/or pressure.[8,9] Further, the synthesis of TMNs involves reaction pathways that are still poorly understood. A deeper understanding of the synthesis and reaction mechanisms is crucial to fully explore the TMN space and develop TMN materials with desired chemical and physical properties with respect to their application.[8,22,23]

Among TMNs, Cu_3N has emerged as a promising material since it is non-toxic and earth-abundant, showing potential for cost-efficient solar energy conversion, catalysis and optoelectronics.[24] Cu_3N exhibits the anti-ReO_3 structure with corner-shared N-centered Cu-N octahedra. The vacant cubic central position can be occupied by a dopant such as Pd forming e.g. Cu_3PdN which changes the electronic structure from semiconducting to semimetallic.[25–29] Cu_3PdN has been proposed to be a node-line semimetal and topological superconductor.[30–32] Further, Cu_3PdN shows good electrochemical catalytic activity and stability for nitrate reduction[33], CO_2 reduction[34,35], O_2 reduction[36] and formic acid oxidation[37]. So far there are no reports on its activity for the hydrogen evolution reaction (HER). Independent of the application, Cu_3PdN exhibits superior catalytic activity and/or stability over the Pd deficient Cu_3N[33,36] as well as N deficient Cu_3Pd[34,37] or Pd[33,36,37] counterparts.

All reported solvothermal synthetic approaches for Cu_3PdN follow the same route: $Cu(NO_3)_2{\cdot}3H_2O$ and $Pd(acac)_2$ form 10 – 20 nm sized Cu_3PdN nanoparticles (NPs) after 5 – 60 min at 230 – 250°C in oleylamine (OAm) and 1-octadecene or hexadecane (Table S1).[33–38] The reaction temperature can be decreased to 190°C if Au, Pt and Pt-Fe_3O_4 NP seeds are used.[39] In the reported synthesis route, OAm is expected to be both reductant and nitrogen source. First OAm is oxidized by the nitrate and Cu(II) to a primary aldimine which reacts with extant OAm to a secondary aldimine, releasing ammonia. Consequently, ammonia reacts with Cu(I) forming Cu_3PdN.[38] This mechanism has been proposed based on the analysis of the reaction byproducts using ^1H nuclear magnetic resonance (NMR), which is sensitive to the organic species present at the end of the reaction, but does not give exhaustive information on the nature of the metal complexes leading to the formation of the Cu_3PdN NPs. Moreover, limited information is given on the phase purity of Cu_3PdN NPs obtained with the OAm route, since the published powder x-ray diffraction (PXRD) patterns display a peak shape anisotropy that likely indicates the presence of bimetallic Cu_3Pd impurities.[33–39]

Here, we report a rapid, one-pot synthesis route that yields phase pure, highly crystalline 3 nm Cu_3PdN NPs. Unlike aforementioned reports on Cu_3PdN synthesis,[33–39] we can decrease the reaction temperature to 140°C by replacing copper (II) nitrate trihydrate with copper (II)

methoxide and dissolving it, jointly with palladium (II) acetylacetonate, in benzylamine instead of OAm. Similar to the Cu_3N synthesis,[40] benzylamine acts as ligand, reductant and nitrogen source.

First, we perform Rietveld refinement and extended x-ray absorption fine structure (EXAFS) analysis of ex situ PXRD and x-ray absorption spectroscopy (XAS) data, respectively, to demonstrate phase purity and to examine the local structure around Cu and Pd in the anti-perovskite Cu_3PdN crystal structure. We find that the as prepared 3 nm Cu_3PdN NPs display cation-site disorder, with the Cu and Pd atoms being distributed at the corners and at the face centers of the cation fcc sublattice, with partial occupancy. This is the first time that cation-site disorder is reported for the case of colloidal TMNs with the anti-perovskite structure.[41–43]
Additionally, using in situ x-ray absorption near-edge spectroscopy (HERFD-XANES) and in situ pair distribution function (PDF) analysis of total scattering (TS), we investigate the reaction pathways involving the Cu and Pd starting complexes during the synthesis of Cu_3PdN in benzylamine. HERFD-XANES is a powerful, element-specific technique that probes the emergence of the electronic structure of a material and monitors the coordination of metal centers during the synthesis, including the formation and transformation of metal-organic complexes and intermediates into the desired crystalline nanomaterial, thereby shedding light on the reaction mechanism.[44,45] Meanwhile, PDF analysis investigates the atomic structure of a material and thus allows to monitor the nucleation and growth of Cu_3PdN NPs.[46] Hence, in situ HERFD-XANES complemented by in situ PDF provides both electronic and structural insights, giving a comprehensive picture of the synthetic pathways together with the appearance of a metallic Cu_3Pd impurities for extended reaction times.
Finally, we test the electrocatalytic properties of the as synthesized Cu_3PdN NPs for the HER, showing good catalytic activity with an overpotential of $\eta_{10} = 212 \pm 11$ mV measured at 10 mA/cm^2 and excellent stability with virtually no change of the overpotential after 10000 linear sweep voltammetry (LSV) cycles. Figure 1 shows a schematic representation of the work conducted in this report.

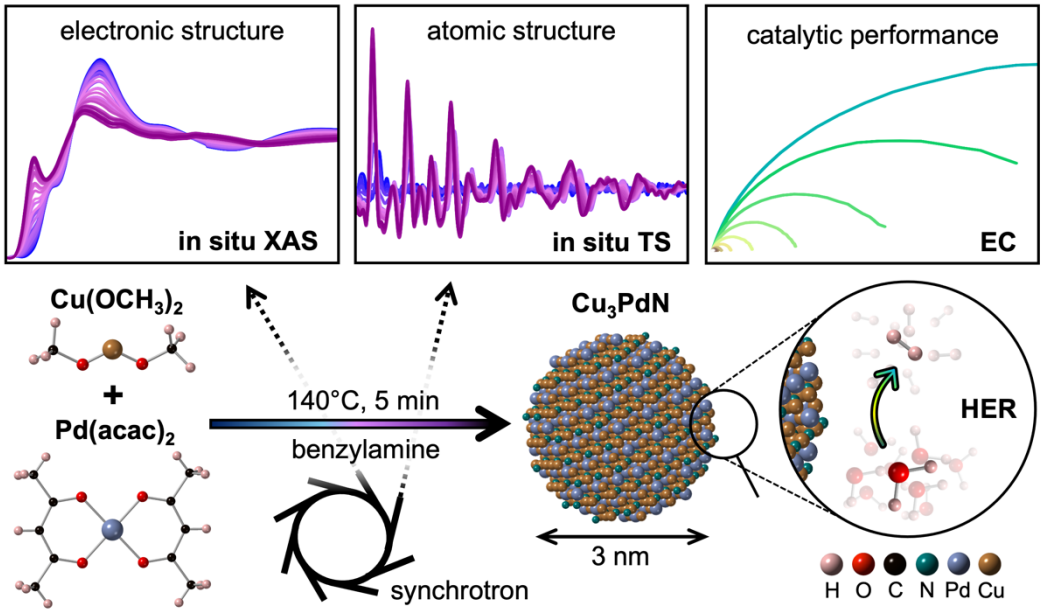

Figure 1: Schematic illustration of the present work. The reaction of Cu(II) methoxide and Pd(II) acetylacetonate, which yields Cu_3PdN nanoparticles after 5 min at 140 °C in benzylamine, is studied using in situ x-ray absorption spectroscopy (XAS) and in situ total scattering (TS). The synthesized Cu_3PdN nanoparticles are tested for their electrochemical (EC) catalytic activity of the hydrogen evolution reaction (HER).

2. Results & Discussion

We perform the solvothermal synthesis of Cu_3PdN nanoparticles by reacting $Cu(OCH_3)_2$ and $Pd(acac)_2$ in benzylamine, which acts both as the solvent and nitrogen source. The reaction is carried out at 140°C under inert atmosphere in a custom-made heating cell that enables precise control of reaction parameters such as the reaction temperature, reaction time, ramp rate and stirring of the reaction.[47] The reaction yields Cu_3PdN nanoparticles with sizes of ~3.5 nm for reaction times of 5 to 15 minutes as shown in Figure S1. Figure 2a shows a high-resolution transmission electron microscopy (HRTEM) image of the Cu_3PdN nanoparticles after 5 minutes reaction time. The identified lattice spacing of 1.9 Å, 2.2 Å and 2.7 Å correspond to the (200), (111), and (110) planes, respectively, and are highlighted in Figure 2b. The corresponding selected area electron diffraction (SAED) pattern displays diffraction peaks with position and intensities consistent with the anti-perovskite crystal structure of Cu_3PdN as shown in Figure 2c. The elemental color mapping with overlay and line scan confirm that the nanoparticles are composed of Cu, Pd and N atoms and their signals overlap uniformly as shown in Figure 2d,e. Figure 2f shows the UV-vis spectra of Cu_3PdN nanoparticles. Unlike previous study that reported an indirect bandgap of 0.2 eV, we observe a direct optical bandgap of 0.61 eV. The discrepancies may arise due to the particle size being four times smaller and, more importantly, the absence of impurities in our sample.[38] Further studies of the optical properties are beyond the scope of this work. The thermogravimetric analysis (TGA) of the obtained Cu_3PdN nanoparticles (Figure S2) depicts a weight loss at low temperature below 160 °C due to the removal of residual organics and a second one at temperature above 250 °C likely due to the reduction of Cu_3PdN to bimetallic/metallic.[38]

Cu_3Pd might form as a secondary phase during the synthesis of Cu_3PdN, thus we first check the phase purity of the obtained Cu_3PdN nanoparticles via Rietveld refinement of the PXRD patterns, as shown in Figure 2g. The PXRD patterns of Cu_3PdN and Cu_3Pd are very similar, with subtle differences in peak intensity and position, since both structures share the same space group and exhibit a slightly different lattice parameter as illustrated in Figure S3. In Figure S4 we simulate two-phase PXRD patterns with different phase ratios of Cu_3PdN:Cu_3Pd. The presence of a Cu_3Pd impurity generates a peak-shape anisotropy, which is most prominently visible at the most intense (111) reflection at around $2\Theta = 41°$ (assuming Cu K-alpha radiation, $q = 2.9$ Å^{-1}). This peak shape anisotropy is present in most of the PXRD patterns of previously reported Cu_3PdN syntheses[33–39],

confirming that the presence of Cu_3Pd impurity is often overlooked. The PXRD patterns of our Cu_3PdN nanoparticles prepared with a reaction time of 5, 10 and 15 minutes are reported in Figure S5 and confirm the absence of Cu_3Pd impurities. The Cu_3Pd phase appears only after reaction times longer than 15 minutes, as also confirmed by our in situ TS study discussed below.

To further confirm the phase purity, we perform EXAFS analysis, which allows to determine the local structure around the absorbing atom.[48] In addition to being an element-specific technique, EXAFS is well suited for multielement materials, allowing to obtain insights such as atomic rearrangements, defects and disorders.

The attempt to refine the ex situ EXAFS data of both Cu and Pd K-edges using the ordered anti-perovskite crystal structure, does not yield a satisfactory agreement, as shown in Figure S6. A careful look at the Fourier-transformed Pd K-edge data (Figure 2i) reveals the presence of a peak around 1.6 Å originating from the scattering contribution of Pd-N distances in the first coordination shell of Pd atoms. This is a clear indication of the presence of a partial short-range cation-site disorder in the Cu_3PdN NPs, where the Cu and Pd atoms are located at the corners and at the face centers of the cation fcc sublattice, with partial occupancy, as shown in Figure 2j. This result is further supported by the oxidation state of the Cu cation. In the ordered structure, the average oxidation state of Cu is +1[38] and it is expected to be < +1 for the structure with cation-site disorder. The maximum of the first derivative of Cu K-edge XANES of Cu_3PdN in Figure S7 is slightly higher (8979.7 eV) than the reference Cu foil (8979.0 eV). However, when compared to the literature value for Cu_3N and Cu_2O (8980.5 eV) in which the oxidation state of Cu is +1[49,50], our sample's edge position is at slightly lower energy (ΔE = 0.8 eV). This clearly emphasizes that the average oxidation state of Cu in Cu_3PdN is < +1, which further hints to the presence of cation-site disorder in our Cu_3PdN NPs. We therefore perform a double-edge EXAFS refinement procedure, utilizing both Cu K-edge and Pd K-edge EXAFS data which allows to simultaneously resolve the local structure around the Cu and Pd atom and to quantitatively assess the cation-site occupancy. The multi-shell fitting method employed uses the physical constraints given by the crystallographic structure, which includes the lattice parameter and the Cu-Pd and Pd-Pd distances. The many-body amplitude reduction factor (S_0^2) and the energy origin shift (ΔE_0) were considered as fixed parameters.[51] The Fourier-transformed EXAFS spectra, and their best fits are shown in Figure 2h and 2i and in Figure S8 and S9. The EXFAS fit of our Cu_3PdN NPs confirms the

presence of partial short-range cation-site disorder where about 25 % of the Pd atoms exchanged their lattice position. The interatomic distances and Debye-Waller factors obtained from the fit can be found in Table S2. This short-range cation-site disorder occurs mainly due to low cation mobility, fast growth rate at the low temperature and short reaction times employed during the synthesis, which favors the formation of the disordered over the ordered structures.[52]

The short- and long-range disorder have already been experimentally observed and theoretically predicted in II-IV-N_2 wurtzite-derived structures[43,53–56] (e.g. $MgSnN_2$, $ZnGeN_2$) and other TMNs.[57–59] The cation-site disorder in the nitride system is highly beneficial and allows to control and tune the properties such as band gap, ion and thermal conductivity.[60,61] Nevertheless, it is important to highlight that this type of cation-site disorder has not been reported before for the case of colloidal anti-perovskite structured nitride systems, especially in Cu_3PdN.

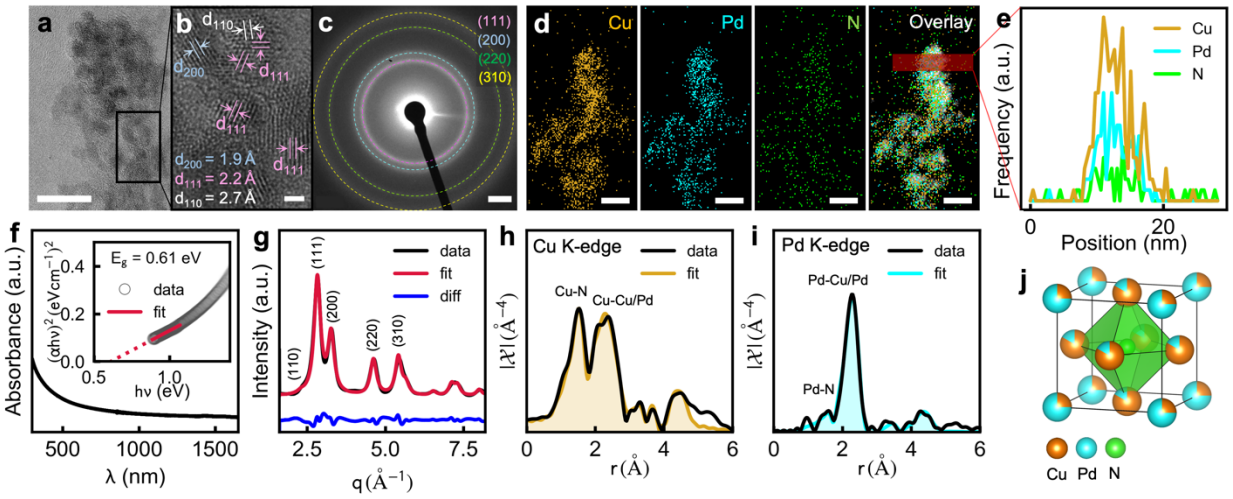

Figure 2: Ex situ characterization of Cu_3PdN NPs grown after 5 min reaction time. a HRTEM of Cu_3PdN NP agglomerate. **b** Zoom of a showing polydisperse spherical NPs. **c** SAED of a Cu_3PdN assembly. **d** STEM:EDX elemental mapping of Cu, Pd and N and an overlay of the mapped elements on the original STEM image. **e** EDX elemental line profiles of the area highlighted in c showing evenly distributed Cu, Pd and N. **f** UV-vis absorption spectrum of Cu_3PdN NPs redispersed in N-methyl-2-pyrrolidon with its corresponding Tauc plot assuming a direct allowed transition as an inset. The dotted red trace shows the extrapolation of the linear fit shown as a solid red trace. **g** PXRD Rietveld refinement. **h** Cu K-edge EXAFS fit. **i** Pd K-edge EXAFS fit. **j** Unit cell of cation-site disordered Cu_3PdN in which the Pd site is partially occupied by Cu and vice versa. Scales: a: 10 nm; b: 1 nm; c: 2 1/nm; d: 10 nm.

The analysis of ex situ PXRD and EXAFS measurements demonstrates the phase purity of the obtained Cu_3PdN NPs and reveals cation-side disorder within the anti-perovskite crystal lattice. To elucidate the reaction pathways leading to the Cu3PdN NPs, Figure 3a, we employ in situ Cu K-edge HERFD-XANES and PDF of in situ TS data. Figure 3b shows the in situ Cu K-edge HERFD-XANES data. The initial spectrum, blue trace, shows the Cu species in the initial reaction solution at room temperature. The last spectrum, purple trace, shows the final product Cu_3PdN after 10 min at 140°C. The reaction solution is heated up to the reaction temperature of 140°C with a heating rate of 10°C/min. The time at which the reaction temperature is reached is defined as 0 min. The room temperature XANES spectrum exhibits a pre-edge peak at 8977 eV, feature A in Figure 3b, which is the fingerprint of Cu^{2+} originating from a dipole-forbidden and quadrupole-allowed 1s-3d transition.[62,63] Feature B at the rising edge, at 8983 eV, is due to the 1s to unoccupied 4p transition.[62,63] A clear intense rising edge transition feature is evident for a square-planar coordination.[64,65] At elevated temperature, the pre-edge, feature A, disappears, while the white-line intensity, feature D, decreases and the edge energy is shifted towards lower energy as indicated by arrows in Figure 3b. This is a clear indication of the reduction of Cu^{2+} and the decrease of the average coordination number in the first coordination shell around Cu. Further, we attribute the simultaneous appearance of two additional features at 8984 eV and 8988 eV, feature C, to the presence of only Cu-N coordination, that leads to the formation of a nitride phase.[66,67]

We apply the multivariate curve resolution by alternating least squares (MCR-ALS) method to the in situ HERD-XANES data and extract the evolution of two distinct Cu components during the reaction, indicating that the initial Cu complex directly reduces to the final Cu_3PdN phase with no intermediates, as soon as the reaction temperature reaches 140°C, as shown in Figure 3c. Their corresponding eigen value profile is shown in Figure S13 while the full-time series of individual Cu K-edge HERFD-XANES spectra, including their MCR-ALS contributions can be found in Figure S14. By comparing the recovered spectra with FEFF[68] simulations, we attribute the starting Cu complex formed when $Cu(OCH_3)_2$ is dissolved in benzylamine ($BnNH_2$) to $[Cu_2(BnNH_2)_4(OCH_3)_2]^{2+}$, Figure 3d left panel. In this complex, two Cu ions are bridged and coordinated with two amine molecules and two methoxy groups in a square planar configuration, as shown in Figure 3a. This complex is similar to the one reported already when CuI is dissolved

in methanol and $BnNH_2$ at room temperature.[69] Additionally, we identify the Pd complex present in the reaction solution at room temperature and Cu_3PdN 10 min after reaching 140°C by ex situ Pd K-edge XANES in Figure 3d right panel. When the $Pd(acac)_2$ is dissolved in $BnNH_2$, the acetylacetonate ligand is released and the Pd^{2+} ion center is coordinated with four $BnNH_2$ molecules in a square-planar configuration forming $[Pd(BnNH_2)_4]^{2+}$, Figure 3a.[70] The Cu K-edge and Pd K-edge XANES spectra of the initial precursors and final product, together with their corresponding FEFF simulated spectra, are shown in Figure 3d.

We complement the in situ HERFD-XANES results with in situ PDF analysis as shown in Figure 3e. Consistently to the HERFD-XANES, PDF analysis shows the prompt formation of Cu_3PdN NPs upon reaching the reaction temperature of 140°C, indicated by the emergence of distinct features at high *r* and the shift of the first peak from ~2.1 to 2.0 Å and second peak from ~2.9 to 2.7 Å. The first and second peak are highlighted in green and orange, respectively, in Figure 3e and the evolution of the peak position is displayed in Figure S16b. The first and second shell interatomic distances, corresponding to the first and second peak in the PDF, are consistently highlighted in the representation of the starting complexes $[Cu_2(BnNH_2)_4(OCH_3)_2]^{2+}$ and $[Pd(BnNH_2)_4]^{2+}$ and the Cu_3PdN unit cell in Figure 3a. Here we assume the ordered anti-perovskite structure without cation-disorder since the PDF hardly has sensitivity to the cation-disorder in a high symmetry structure like Cu_3PdN as shown by PDF simulations in Figure S16.
The in situ PDF data is compared to PDF simulations of the starting complexes and the Cu_3PdN phase shown as dashed traces in Figure 3e. The initial PDF, blue trace, matches the superposition of the PDF simulations of the Cu and Pd complex, and the last PDF, purple trace, matches the PDF simulation of phase-pure Cu_3PdN as shown in Figure 3e. In Figure S16c we analyze the in situ PDF by a linear combination of the initial PDF and the final PDF, which shows consistent reaction pathways to the MCR-ALS findings of Cu K-edge HERFD-XANES. Figure S18 shows the full time-series of the individual PDFs. A detailed description of the analysis procedures and data processing routines are given in the supporting information.

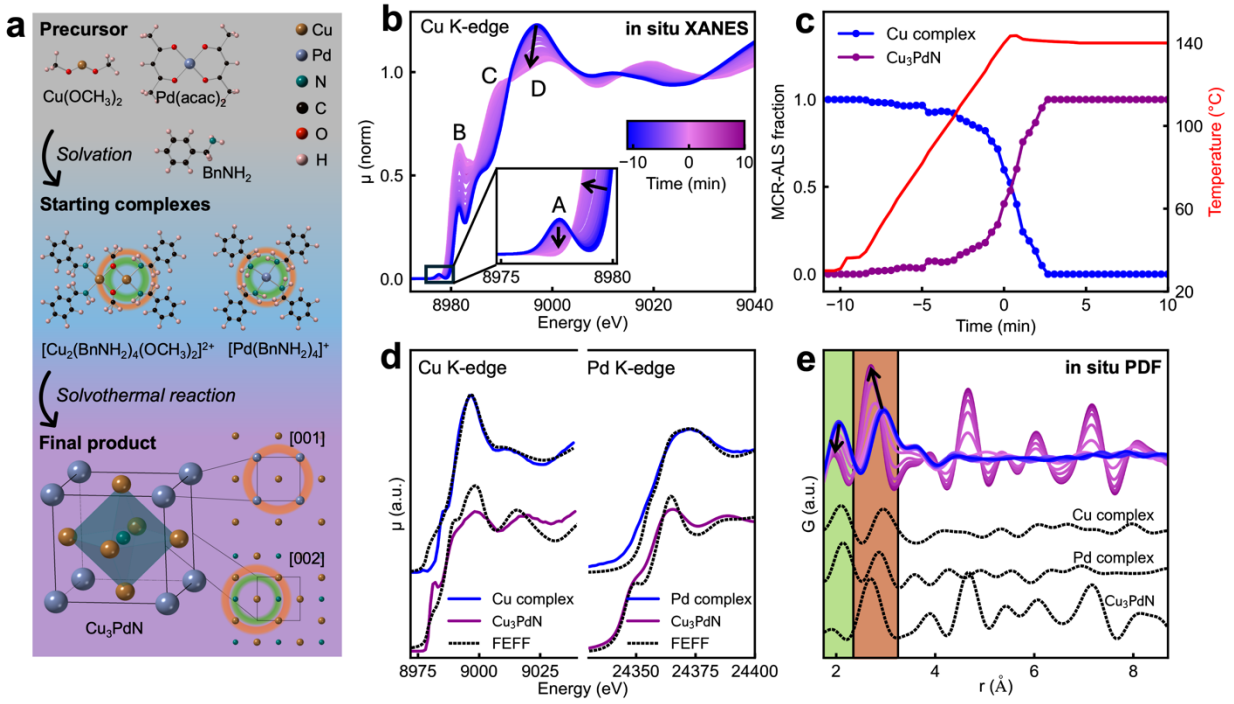

Figure 3: In situ XANES and PDF analysis of the reaction to Cu_3PdN. a Schematic of reaction mechanism. The $Cu(OCH_3)_2$ and $Pd(acac)_2$ precursors dissolve in benzylamine to form $[Cu_2(BnNH_2)_4(OCH_3)_2]^{2+}$ and $[Pd(BnNH_2)_4]^{+}$ complexes, respectively, which upon heating form Cu_3PdN. The first shell and second shell around the metal atoms are highlighted by green and orange circles, respectively. **b** In situ Cu K-edge HERFD-XANES data and **c** corresponding MCR-ALS analysis of the in situ Cu K-edge HERFD-XANES show the formation of Cu_3PdN from the Cu starting complex without intermediates. **d** XANES spectra of the starting complexes and Cu_3PdN at Cu K-edge and Pd K-edge compared to FEFF simulations. The left panel shows the recovered spectra of the Cu starting complex and final product Cu_3PdN from MCR-ALS analysis. The right panel shows ex situ XANES spectra of Pd starting complex and Cu_3PdN. The spectra are in good agreement with the FEFF simulations of the respective structures. **e** In situ PDFs G(r). The in situ PDF data is compared to PDF simulations of the Cu and Pd starting complexes and Cu_3PdN phase in dashed black traces.

For reaction times exceeding 15 minutes at 140°C, in situ time-resolved PDF refinements (Figure S19-21) reveal a further reduction of Cu_3PdN to the metallic Cu_3Pd phase, which completes within 40 minutes. The phase transformation is indicated by a peak shift to lower *r,* corresponding to a decrease in the lattice constant as nitrogen atoms leave the crystal lattice. In this context, our ex

situ PXRD and EXAFS characterization, combined with in situ XANES and PDF analysis, provides a comprehensive view of the reaction pathway during synthesis, highlighting that an accurate control of the reaction parameters is needed to achieve phase pure Cu_3PdN NPs.

Phase purity is particularly important when evaluating the electrocatalytic performance of a material. For example, Cu_3PdN has shown superior electrochemical activity for processes such as CO_2 reduction[34] and formic acid oxidation[37] compared to the metallic Cu_3Pd phase. Interestingly, the electrocatalytic performance of Cu_3PdN NPs for the HER, the cathodic compartment of a water splitting cell, has not been reported so far. We therefore deposited our Cu_3PdN NPs on a glassy carbon electrode and tested their electrochemical performance for the HER in acidic media, using a 0.5 M H_2SO_4 aqueous solution as the electrolyte. For comparison, the bare glassy carbon electrode and 20 wt% Pt/C deposited on glassy carbon with the same catalyst loading were also tested under the same conditions. The linear sweep voltammetry (LSV) scan in Figure 4a reveals an overpotential of $\eta_{10} = 212 \pm 11$ mV measured at 10 mA/cm^2 and an onset potential of $\eta_1 = 67 \pm 12$ mV defined at 1 mA/cm^2. The Tafel plot in Figure 4b displays a slope of 125 mV/dec suggesting that the HER on Cu_3PdN follows the two-step Volmer-Heyrovský mechanism:[71]

$$H_3O^+ + 1e^- \rightleftharpoons H_{ads} + H_2O \text{ (Volmer reaction)} \quad (1)$$

$$H_3O^+ + H_{ads} + 1e^- \rightleftharpoons H_2 + H_2O \text{ (Heyrovský reaction)} \quad (2)$$

where in the first step (1) protons are discharged to form adsorbed hydrogen (H_{ads}) followed by the electrochemical desorption of an H_2 molecule during the second step (2). A Tafel slope close to 120 mV/dec is often attributed to the Volmer reaction being the rate-determining step, although recent studies also suggest that such a slope can be obtained for the Heyrovský reaction being the rate-determining step when the surface of the catalyst is highly covered with adsorbed hydrogen species.[72] We also determine the double layer capacitance (C_{dl}) of the electrode from cycling voltammetry measurements as shown in Figures 4c and S21, suggesting that the Cu_3PdN NPs display a high number of active site and an electrochemically active surface area (ECSA) about 21 times higher than the bare glassy carbon electrode. We further assess the stability of the Cu_3PdN NPs during HER operation as shown in Figure 4d. We perform 10000 repeated LSV cycles and recorded a small cathodic shift of about 5 mV after refreshing the electrolyte, suggesting that the

Cu_3PdN NPs show remarkable stability during HER operation. We further investigate the charge transfer kinetics at the electrode-electrolyte interface via electrochemical impedance spectroscopy (EIS). In Figure 4e we show a typical Nyquist plot, displaying the presence of a single semicircle with decreasing diameter moving to more cathodic potentials, which suggests that the process is dominated by a charge transfer resistance with the absence of additional processes such as diffusion and mass transport limitations. We model the data with a simple equivalent circuit comprising a resistor (Rs) in series with a parallel combination of a charge transfer resistance (R_{CT}) and a constant phase element as shown in Figure S23. Figure 4f shows the dependence of the obtained R_{CT} as a function of the applied potential. At the overpotential of η_{10} = 212 mV, R_{CT} drops to 9.5 Ω, indicating an efficient charge transfer resistance at the catalyst-electrolyte interface. We further obtain a Tafel plot utilizing the R_{CT} extracted from the EIS fitting (inset in Figure 4f), revealing a slope of 125 mV/dec, which is identical to the one obtained with the voltammetric analysis. This indicates that the HER at the surface of Cu_3PdN proceeds under pure charge transfer kinetics, without limitations arising from mass transfer diffusion.

Figure 4g presents a comparative overview of the overpotentials and Tafel slopes reported in the literature for various nitrides during HER. The activity of the Cu_3PdN NPs obtained in this study compares favorably with that of other reported metal nitrides, as the overpotential of most tested nitrides falls within the range of 100 – 250 mV. It is noteworthy that many of the reported nitrides are either supported on a porous substrate (e.g. Ni_2N on nickel foam[73]) or are synthesized as composites (e.g. Mo_2N-Mo_2C[74–76]). These strategies effectively lower the overpotential required for the HER, by utilizing a catalyst support with a very large surface area or by leveraging the synergistic catalytic properties of composite heterostructures. Adopting these approaches could further enhance the performance of Cu_3PdN in future studies. Nevertheless, our findings indicate that phase pure Cu_3PdN NPs are a promising electrocatalyst for the HER in acidic media.

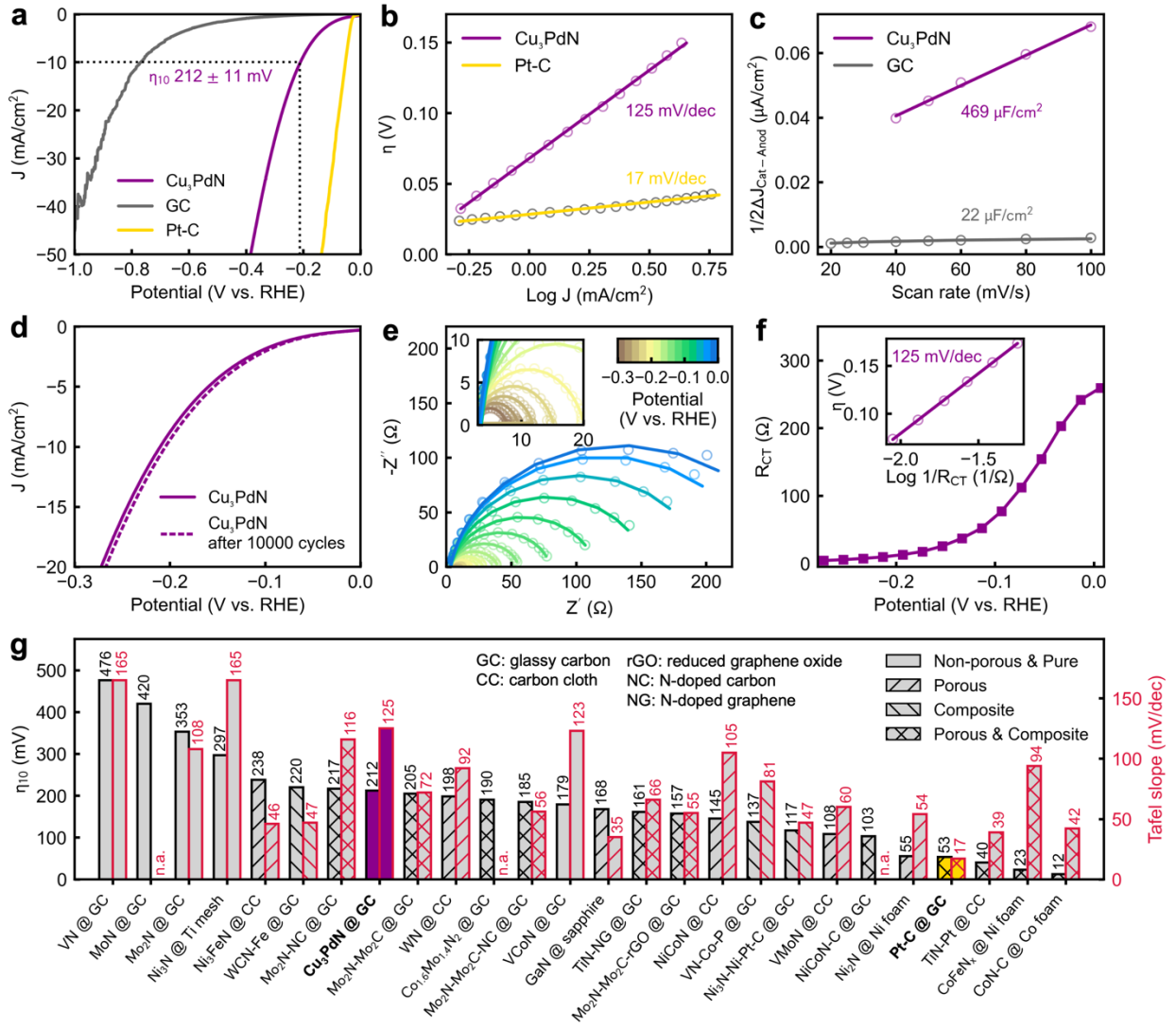

Figure 4: Electrocatalytic performance of Cu_3PdN NPs for the HER. a Typical LSV curve of Cu_3PdN NPs deposited on glassy carbon, compared with Pt-C and bare glassy carbon electrode, measured at a scan rate of 10 mV/s. **b** Tafel plot obtained from the LSV curves. **c** double layer capacitances obtained from the half-slope of the capacitive currents extracted from cyclic voltammetry measurements at increasing scan rates. **d** LSV scans before and after 10000 LSV cycles to assess the stability of the electrode. **e** Nyquist plot obtained via EIS measurements. **f** Dependence of the charge transfer resistance obtained by fitting the EIS data, along with the Tafel plot obtained using the R_{CT} extracted from the impedance fitting (inset). **g** Comparison of the obtained overpotential and Tafel slope, highlighted with a colored bar and bold label, with other

transition metal nitrides from the literature; missing data points are noted as n.a.: not available.[73–95] A detailed overview is given in Table S9.

3. Conclusion

This study presents the one-pot synthesis of phase-pure, highly crystalline Cu_3PdN NPs with an average size of 3 nm using benzylamine as a solvent at 140°C, which is, so far, the lowest reported reaction temperature for Cu_3PdN synthesis. The Rietveld refinement of the ex situ PXRD patterns demonstrates the phase purity of the obtained Cu_3PdN NPs, shedding light on the occurrence of Cu_3Pd impurities often overlooked in previous reports. Crucially, the double-edge EXAFS analysis reveals the occurrence of disorder in the anti-perovskite crystal lattice, with about 25% of the Pd atoms interchanging their position with adjacent Cu atoms, generating a disordered structure with partial cation-site occupancy. The ability to control the cation-site disorder through parameters such as heating rate, reaction temperature and time or precursor concentrations could enable to tailor properties like the band gap, electronic conductivity and electrocatalytic activity. Additionally, tuning those reaction parameters could impact the size and size distribution of the Cu_3PdN NPs. The significantly smaller size of the synthesized Cu_3PdN NPs, less than half of the previously reported colloidal Cu_3PdN, provides a high surface area, making them highly suitable for application in electrocatalysis. We showcase that Cu_3PdN is suitable for the HER, revealing remarkable stability and an overpotential of 212 ± 11 mV at 10 mA/cm^2 which is comparable to many other reported nitride catalysts. Supporting Cu_3PdN on porous substrates with a large surface area such as Ni foam could be a strategy to further lower the overpotential required for the HER.

We further monitor the reaction pathway leading to the formation of Cu_3PdN NPs in benzylamine, employing in situ HERFD-XANES and PDF analysis of in situ TS data. We observe that the solvation of the Cu and Pd precursors leads to the formation of $[Cu_2(BnNH_2)_4(OCH3)_2]^{2+}$ and $[Pd(BnNH_2)_4]^{2+}$ as starting complexes which then directly react and convert to Cu_3PdN immediately after reaching the reaction temperature of 140 °C. For an extended reaction time (>15 min), further reduction of Cu_3PdN to bimetallic Cu_3Pd occurs, emphasizing that a meticulous control of the reaction parameters can prevent the formation of impurities.

In conclusion, our study offers comprehensive insights into the structural and mechanistic aspects of Cu_3PdN NP formation. The methodologies and findings presented here can be applied to other

TMNs, opening avenues for optimizing their properties and expanding their potential applications in energy conversion and beyond.

4. Experimental Section

Chemicals

All Chemicals were purchased from commercial sources and used without further purification: $Cu(OCH_3)_2$ (Thermo Scientific, 98%), $Pd(acac)_2$ (Sigma Aldrich, 99%), benzylamine (Sigma Aldrich, 99%), hexane (Sigma Aldrich, 99%), N-methyl-2-pyrrolidon (VWR, 99.8%), H_2SO_4 (Carl Roth, 96%), methanol (VWR, 99.8%), NAFION (Ion-Power, 5% in methanol). All chemicals used for the syntheses were stored and handled in the glove box under inert atmosphere (Ar 6.0, $c(H_2O) > 0.1$ ppm, $c(O_2) > 0.1$ ppm).

Synthesis

In a typical synthesis a stock solution is prepared in the glove box by adding $Cu(OCH_3)_2$ (37.7 mg, 0.3 mmol) and $Pd(acac)_2$ (30.5 mg, 0.1 mmol) to 5 mL of benzylamine and stirring until all precursors are dissolved. Subsequently, a quantity of 2.5 mL was transferred to the inlet of the heating cell. Instead, for in situ reactions, a quantity of 0.3 mL was transferred to the respective reaction container for in situ XAS or in situ TS, respectively, as explained below. Consequently, the reaction container was assembled in the heating cell, taken out of the glovebox and heated to 140°C with a heating rate of 10°C/min under vigorous stirring. After the desired reaction time at 140°C the heating cell was cooled to room temperature.

After the synthesis, the NPs were washed 3 times with hexane and centrifuged for 10 min at 10000 rpm. After the last centrifugation step, the nanocrystals were dried under nitrogen flow.

The NP dispersion for HRTEM, STEM:EDX, STEM and UV-vis characterization were prepared by redispersing the NPs in N-methyl-2-pyrrolidon after the last centrifugation step and discarding the supernatant before drying under nitrogen flow to prevent agglomeration of the synthesized NPs.

Heating cell

The synthesis is carried out in a custom-made heating cell which enables precise control of the ramp rate, reaction temperature and reaction time, allows for stirring and operates under solvothermal conditions. The heating cell consists of a metal body and isolating polyether ether ketone (PEEK) (Bieglo) elements. Four heating elements (Cartridge heaters, 24 V, 50 W, Maxiwatt) and a temperature sensor (Pt1000, Honeywell) were used to control the temperature

with a temperature controller (Model 336, Lakeshore Cryotronics) and a power supply (EA-PS 310060-340, Elektro-Automatik). For the reaction, the heating cell is mounted on top of a magnetic stirring motor (Cimarec i, Thermo Scientific). The reaction takes place in a PEEK inlet as reaction container. The heating cell is also used for in situ XAS and in situ TS experiments. In situ XAS experiments take place in a PEEK inlet with 0.2 mm wall thickness in reflection geometry. In situ TS experiments take place in a fused silica inlet with 0.5 mm wall thickness in transmission geometry. The heating cell is discussed in detail in the literature.[47]

We note that the synthesis is also feasible in a conventional autoclave. However, the reaction requires vigorous stirring in addition to an inert atmosphere which can be achieved by placing the reaction solution and a stirring magnet in the autoclave and heating the autoclave in an oil bath on a magnetic stirring plate.

In situ High Energy Resolution Fluorescence Detected X-ray Absorption Near Edge Structure (HERFD-XANES)

In situ Cu K-edge HERFD-XANES measurements were performed at ID26[96] and ID24 beamlines of the European Synchrotron Radiation Facility (ESRF), Grenoble, France. The incident x-ray energy was chosen using the reflection from the Si(111) double crystal monochromator (DCM) and varied from 8970 to 9060 eV at ID26 and 8970-9040 eV at ID24 using Si(311) DCM. The spectra were acquired in fluorescence mode, detecting only photons whose energy corresponded to the maximum intensity of the Cu K-α_1 emission line (8046 eV) with an emission spectrometer in Rowland geometry with spherically bent Si(444) five analyzing crystals[97] aligned at the Bragg angle of 79.4°. The HERFD-XANES spectra were recorded in a continuous scan mode every 20-25 s in the energy range of 8970-9060 eV with a step size of 0.2 eV. The overall energy resolution is about 1.70 eV of FWHM at the Cu K K-α_1 emission line. The beam spot size was about 200*200 µm and the beam position on the cell was moved after 2-5 scans to avoid the sample damage due to the long exposure to x-rays. The details of the beam damage study can be found in the SI. The ex situ powder samples were measured as pellet diluting with cellulose.

The Pd K-edge (24350 eV) EXAFS data were acquired in a transmission mode at the P64 beamline[98] of the PETRA III, DESY in Hamburg, Germany. Si (111) monochromator was used for scanning the x-ray energy from 24135-24060 eV.

The EXAFS of Cu_3PdN powder samples were measured both at Cu and Pd K-edges at the BM23 beamline[99] of the ESRF, Grenoble, France. All the measurements were taken in transmission mode on pressed pellets diluted with cellulose. The samples were placed between the gas-filled ionization chambers I_0 and I_1. Si (311) DCM was used to monochromatize the incident beam. The spectra were energy calibrated using respective metallic foils as reference placed after the I1 ionization chamber and the transmitted x-ray intensity by foil was measured using a third ionization chamber (I_2). All the spectra were averaged over three scans to improve the quality of the spectra.

A detailed description of the XANES, EXAFS and MCR-ALS analysis procedures is given in the supporting information.

In situ Total Scattering (TS) and Pair Distribution Function (PDF) analysis

In situ TS data was acquired at beamline P21.1 of PETRA III at Deutsches Elektronen-Synchrotron DESY, Hamburg, Germany. Scattering images were recorded every 1 s at an x-ray energy of 101.39 keV ($\lambda = 0.1222$ Å) using a 2D X-ray detector (PerkinElmer XRD1621, Varex Imaging Corp.) with 2048x2048 pixels and a pixel size of 200 × 200 μm² and a sample-to-detector distance of 0.604 m, obtained from a calibration with a LaB_6 powder standard packed into the fused silica inlet of the heating cell.

A detailed description of the PDF analysis procedures is given in the supporting information. The code used for data processing of the PDF data is available at https://gitlab.rrz.uni-hamburg.de/BAS0906/shm_2024_cu3pdn.

Electrochemical characterization

The working electrode for the electrochemical measurements was prepared by deposition of the NPs onto an L-shaped glassy carbon electrode with a surface area of 0.78 cm^2. Specifically, 40 μL of a 2 mg/mL dispersion of Cu_3PdN in methanol were drop-casted for six times onto the glassy carbon electrode. Afterwards, a NAFION solution was prepared by mixing 290 μL of methanol with 2 μL of a 5% NAFION dispersion in methanol. 40 μL of the obtained NAFION dispersion were drop-casted onto the glassy carbon electrode with the Cu_3PdN nanoparticles for three times. All the electrochemical measurements were conducted in 0.5M H_2SO_4 employing the typical three-

electrode configuration using a graphite rod and an Ag/AgCl (3M KCl) as counter and reference electrodes, respectively. Prior to the measurement, the electrolyte was degassed by flushing Ar for about 15 minutes. The polarization curves were recorded by liner-sweep voltammetry at a scan rate of either 10 or 1 mV/s in a potential range of 0 to -1 V vs. RHE. All polarization curves were not corrected for iR drop. The double-layer capacitances (C_{dl}) were estimated by cyclic voltammetry using a previously reported method.[100] Cyclic voltammetry scans were carried out in a 60 mV potential window around the open circuit potential, where no Faradaic processes occur, with variable scan rates, from 10 to 100 mV/s. The double-layer capacitances (C_{dl}) were extracted from the half slope of the linearly fitted curves of the capacitive currents ($J_{anodic} - J_{cathodic}$) versus the scan rates. EIS measurements were carried out in a potential window from 0 to -0.35 V vs. RHE with a potential step of 20 mV, an AC sinus amplitude of 10 mV (mean square root voltage V_{rms} = 7.07 mV), a frequency range of 100 kHz – 0.1 Hz and an equilibration time of 30 s between each potential step. The EIS spectra were fitted using the software EC-Lab from Biologic. For all the electrochemical measurements, the potentials acquired with the Ag/AgCl reference electrodes were converted to the RHE scale using the equation E (V vs. RHE) = E (V vs. Ag/AgCl (3 M KCl)) + 0.197 + 0.059 × pH. All electrochemical measurements were recorded using a Biologic SP-150 potentiostat.

Powder X-ray Diffraction (PXRD) & Rietveld Refinement

PXRD patterns were acquired on a Bruker Advanced D8 with Cu K_α-radiation of 8.0478 keV (λ = 1.5406 Å). Rietveld refinements and PXRD simulations were carried out with GSASII.[101] Instrumental parameters have been retrieved by refining a LaB_6 standard.

High-Resolution Transmission Electron Microscopy (HRTEM)

HRTEM images were collected using a JEOLJEM-2200FS (JEOL Ltd.) with an acceleration voltage of 200 kV. The synthesized sample was dispersed in N-methyl-2-pyrrolidon and deposited on a gold grid.

STEM:EDX

STEM:EDX images were collected using a Regulus 8220 (Hitachi High Technologies Corp.) with an acceleration voltage of 30 kV and the BFSTEM acquisition mode.

UV-vis:

UV-visible spectra were collected with a Cary 60 UV-vis spectrometer (Agilent Technologies Inc.) in a quartz cuvette. The sample was dispersed in N-methyl-2-pyrrolidon.

Acknowledgements

This research was supported by the European Research Council (LINCHPIN project, grant no. 818941), the Deutsche Forschungsgemeinschaft (DFG) through the Cluster of Excellence "Advanced Imaging of Matter" (EXC 2056, project ID 390715994) and by the Bundesministerium für Bildung und Forschung (BMBF) via the project 05K22GU7 (LUCENT II). We acknowledge Marvin Skiba and Moritz Dybowski for TGA and UV-vis measurements, respectively. We also acknowledge DESY (Hamburg, Germany), a member of the Helmholtz Association, and ESRF (Grenoble, France) for the provision of experimental facilities. Parts of this research were carried out at PETRA III using beamlines P21.1 and P64 and at ESRF using beamlines ID26, ID24 and BM23 under proposals MA5366 and HC-4929 (*doi.org/10.15151/ESRF-ES-657465136*, *doi.org/10.15151/ESRF-ES-1442330861*). We thank the beamline staff for the support with the experiments: at ID26 Dr. Pieter Glatzel, at P21.1 Dr. Fernando Igoa Dr. Jiatu Liu and at P64 Dr. Wolfgang Caliebe.

References

1. Sun, W. *et al.* A map of the inorganic ternary metal nitrides. *Nat. Mater.* **18**, 732–739 (2019).
2. Yang, Z.-G. *et al.* Recent progress in the synthesis of transition metal nitride catalysts and their applications in electrocatalysis. *Nanoscale* **15**, 11777–11800 (2023).
3. Jamil, R. *et al.* The role of nitrogen in transition-metal nitrides in electrochemical water splitting. *Chem Catalysis* **1**, 802–854 (2021).
4. Calais, J.-L. Band structure of transition metal compounds. *Advances in Physics* **26**, 847–885 (1977).
5. Lengauer, W. & Eder, A. Nitrides: Transition Metal Solid-State Chemistry. in *Carbides: Transition Metal Solid State Chemistry* 3515–3531 (2005). doi:10.1002/0470862106.ia156.
6. Papaconstantopoulos, D. A., Pickett, W. E., Klein, B. M. & Boyer, L. L. Electronic properties of transition-metal nitrides: The group-V and group-VI nitrides VN, NbN, TaN, CrN, MoN, and WN. *Phys. Rev. B* **31**, 752–761 (1985).
7. Xie, J. & Xie, Y. Transition Metal Nitrides for Electrocatalytic Energy Conversion: Opportunities and Challenges. *Chemistry – A European Journal* **22**, 3588–3598 (2016).
8. Wang, H. *et al.* Transition metal nitrides for electrochemical energy applications. *Chem. Soc. Rev.* **50**, 1354–1390 (2021).
9. Zhong, Y. *et al.* Transition Metal Carbides and Nitrides in Energy Storage and Conversion. *Advanced Science* **3**, 1500286 (2016).
10. Han, Y., Yue, X., Jin, Y., Huang, X. & Shen, P. K. Hydrogen evolution reaction in acidic media on single-crystalline titanium nitride nanowires as an efficient non-noble metal electrocatalyst. *J. Mater. Chem. A* **4**, 3673–3677 (2016).

11. Wu, Z. *et al.* Molecularly Thin Nitride Sheets Stabilized by Titanium Carbide as Efficient Bifunctional Electrocatalysts for Fiber-Shaped Rechargeable Zinc-Air Batteries. *Nano Lett.* **20**, 2892–2898 (2020).
12. Vadahanambi, S. & Park, H. Carbon sheathed molybdenum nitride nanoparticles anchored on reduced graphene oxide as high-capacity sodium-ion battery anodes and supercapacitors. *New J. Chem.* **42**, 5668–5673 (2018).
13. Liu, B. *et al.* Unconventional Nickel Nitride Enriched with Nitrogen Vacancies as a High-Efficiency Electrocatalyst for Hydrogen Evolution. *Advanced Science* **5**, 1800406 (2018).
14. Jin, H. *et al.* Nitrogen Vacancies on 2D Layered W_2N_3: A Stable and Efficient Active Site for Nitrogen Reduction Reaction. *Advanced Materials* **31**, 1902709 (2019).
15. Xiong, J. *et al.* Salt-templated synthesis of defect-rich MoN nanosheets for boosted hydrogen evolution reaction. *J. Mater. Chem. A* **5**, 24193–24198 (2017).
16. Yan, H. *et al.* Phosphorus-Modified Tungsten Nitride/Reduced Graphene Oxide as a High-Performance, Non-Noble-Metal Electrocatalyst for the Hydrogen Evolution Reaction. *Angewandte Chemie International Edition* **54**, 6325–6329 (2015).
17. Chen, Z. *et al.* Tailoring the d-Band Centers Enables Co4N Nanosheets To Be Highly Active for Hydrogen Evolution Catalysis. *Angewandte Chemie International Edition* **57**, 5076–5080 (2018).
18. Song, F. *et al.* Interfacing nickel nitride and nickel boosts both electrocatalytic hydrogen evolution and oxidation reactions. *Nat Commun* **9**, 4531 (2018).
19. Li, Q. *et al.* All Hierarchical Core–Shell Heterostructures as Novel Binder-Free Electrode Materials for Ultrahigh-Energy-Density Wearable Asymmetric Supercapacitors. *Advanced Science* **6**, 1801379 (2019).

20. Balamurugan, J., Nguyen, T. T., Aravindan, V., Kim, N. H. & Lee, J. H. Flexible Solid-State Asymmetric Supercapacitors Based on Nitrogen-Doped Graphene Encapsulated Ternary Metal-Nitrides with Ultralong Cycle Life. *Advanced Functional Materials* **28**, 1804663 (2018).
21. Zhu, L. *et al.* Lower ammoniation activation energy of CoN nanosheets by Mn doping with superior energy storage performance for secondary ion batteries. *Nanoscale* **10**, 5581–5590 (2018).
22. Gao, B. *et al.* Recent progress in nanostructured transition metal nitrides for advanced electrochemical energy storage. *J. Mater. Chem. A* **7**, 14–37 (2019).
23. Tareen, A. K., Priyanga, G. S., Behara, S., Thomas, T. & Yang, M. Mixed ternary transition metal nitrides: A comprehensive review of synthesis, electronic structure, and properties of engineering relevance. *Progress in Solid State Chemistry* **53**, 1–26 (2019).
24. Paredes, P., Rauwel, E. & Rauwel, P. Surveying the Synthesis, Optical Properties and Photocatalytic Activity of Cu_3N Nanomaterials. *Nanomaterials* **12**, 2218 (2022).
25. Hahn, U. & Weber, W. Electronic structure and chemical-bonding mechanism of Cu_3N, Cu_3NPd, and related Cu(I) compounds. *Phys. Rev. B* **53**, 12684–12693 (1996).
26. Ji, A., Yun, D., Gao, L. & Cao, Z. Crystalline thin films of stoichiometric Cu_3N and intercalated Cu_3NM_x (M = metals): Growth and physical properties. *physica status solidi (a)* **207**, 2769–2780 (2010).
27. Cui, X. Y. *et al.* First principles study of 3*d* transition metal doped Cu_3N. *Journal of Magnetism and Magnetic Materials* **324**, 3138–3143 (2012).
28. Caskey, C. M., Richards, R. M., Ginley, D. S. & Zakutayev, A. Thin film synthesis and properties of copper nitride, a metastable semiconductor. *Mater. Horiz.* **1**, 424–430 (2014).

29. Jiang, A. Preparation, structure, properties, and application of copper nitride (Cu_3N) thin films: A review. *Journal of Materials Science* 7 (2018).

30. Yu, R., Weng, H., Fang, Z., Dai, X. & Hu, X. Topological Node-Line Semimetal and Dirac Semimetal State in Antiperovskite Cu_3PdN. *Phys. Rev. Lett.* **115**, 036807 (2015).

31. Quintela, C. X. *et al.* Epitaxial thin films of Dirac semimetal antiperovskite Cu_3PdN. *APL Materials* **5**, 096103 (2017).

32. Wang, X., Chen, J. & Xie, D. Prospect of Node-Line Semimetal Cu_3PdN to Be a Topological Superconductor. *J Supercond Nov Magn* **30**, 2727–2734 (2017).

33. Yao, K. *et al.* Regulating charge distribution of Cu_3PdN nanocrystals for nitrate electroreduction to ammonia. *Chem. Commun.* **59**, 12176–12179 (2023).

34. Jia, J., Hao, X., Chang, Y., Jia, M. & Wen, Z. Rational design of Cu_3PdN nanocrystals for selective electroreduction of carbon dioxide to formic acid. *Journal of Colloid and Interface Science* **586**, 491–497 (2021).

35. Li, T. *et al.* Cu_3Pd_xN nanocrystals for efficient CO_2 electrochemical reduction to methane. *Electrochimica Acta* **371**, 137793 (2021).

36. Vaughn II, D. D. *et al.* Solution Synthesis of Cu_3PdN Nanocrystals as Ternary Metal Nitride Electrocatalysts for the Oxygen Reduction Reaction. *Chem. Mater.* **26**, 6226–6232 (2014).

37. Jia, J., Shao, M., Wang, G., Deng, W. & Wen, Z. Cu_3PdN nanocrystals electrocatalyst for formic acid oxidation. *Electrochemistry Communications* **71**, 61–64 (2016).

38. Parvizian, M. *et al.* The Chemistry of Cu_3N and Cu_3PdN Nanocrystals**. *Angewandte Chemie International Edition* **61**, e202207013 (2022).

39. Lord, R. W., Holder, C. F., Fenton, J. L. & Schaak, R. E. Seeded Growth of Metal Nitrides on Noble-Metal Nanoparticles To Form Complex Nanoscale Heterostructures. *Chem. Mater.* **31**, 4605–4613 (2019).

40. Deshmukh, R. *et al.* Ultrasmall Cu_3N Nanoparticles: Surfactant-Free Solution-Phase Synthesis, Nitridation Mechanism, and Application for Lithium Storage. *Chem. Mater.* 7 (2015).

41. Sharan, A. & Lany, S. Computational discovery of stable and metastable ternary oxynitrides. *The Journal of Chemical Physics* **154**, 234706 (2021).

42. Zakutayev, A. Synthesis of Zn_2NbN_3 ternary nitride semiconductor with wurtzite-derived crystal structure. *J. Phys.: Condens. Matter* **33**, 354003 (2021).

43. Rom, C. L. *et al.* Combinatorial Synthesis of Cation-Disordered Manganese Tin Nitride $MnSnN_2$ Thin Films with Magnetic and Semiconducting Properties. *Chem. Mater.* **35**, 2936–2946 (2023).

44. Grote, L. *et al.* X-ray studies bridge the molecular and macro length scales during the emergence of CoO assemblies. *Nat Commun* **12**, 4429 (2021).

45. Glatzel, P. & Bergmann, U. High resolution 1s core hole X-ray spectroscopy in 3d transition metal complexes—electronic and structural information. *Coordination Chemistry Reviews* **249**, 65–95 (2005).

46. Christiansen, T. L., Cooper, S. R. & Jensen, K. M. Ø. There's no place like real-space: elucidating size-dependent atomic structure of nanomaterials using pair distribution function analysis. *Nanoscale Adv.* **2**, 2234–2254 (2020).

47. Klemeyer, L. *et al.* Combining high X-ray energy photon-in photon-out spectroscopies and X-ray scattering to experimentally assess the emergence of electronic- and atomic structure of ZnS nanorods. Preprint at https://doi.org/10.26434/chemrxiv-2024-qflhf (2024).
48. Fornasini, P. Introduction to X-Ray Absorption Spectroscopy. in *Synchrotron Radiation: Basics, Methods and Applications* (eds. Mobilio, S., Boscherini, F. & Meneghini, C.) 181–211 (Springer, Berlin, Heidelberg, 2015). doi:10.1007/978-3-642-55315-8_6.
49. Xu, H., Yamaguchi, S., Mitsudome, T. & Mizugaki, T. A copper nitride nanocube catalyst for highly efficient hydroboration of alkynes. *Organic & Biomolecular Chemistry* **21**, 1404–1410 (2023).
50. Bijani, S. *et al.* XAS study of the reversible reactivity mechanism of micro- and nanostructured electrodeposited Cu_2O thin films towards lithium. *Journal of Materials Chemistry* **21**, 5368–5377 (2011).
51. Mijit, E. *et al.* Structural and electronic transformations of $GeSe_2$ glass under high pressures studied by X-ray absorption spectroscopy. *Proc Natl Acad Sci U S A* **121**, e2318978121 (2024).
52. Schnepf, R. R. *et al.* Utilizing Site Disorder in the Development of New Energy-Relevant Semiconductors. *ACS Energy Letters* **5**, 2027–2041 (2020).
53. Fioretti, A. N. *et al.* Combinatorial insights into doping control and transport properties of zinc tin nitride. *J. Mater. Chem. C* **3**, 11017–11028 (2015).
54. Huang, J. & Kang, J. Cation disorder in $MgSnN_2$ and its effects on the electronic properties. *Phys. Rev. Materials* **8**, 074604 (2024).
55. Melamed, C. L. *et al.* Combinatorial investigation of structural and optical properties of cation-disordered $ZnGeN_2$. *J. Mater. Chem. C* **8**, 8736–8746 (2020).

56. Schnepf, R. R. *et al.* Using resonant energy X-ray diffraction to extract chemical order parameters in ternary semiconductors. *J. Mater. Chem. C* **8**, 4350–4356 (2020).

57. Sirotti, E. *et al.* Beyond Cation Disorder: Site Symmetry-Tuned Optoelectronic Properties of the Ternary Nitride Photoabsorber $ZrTaN_3$. *Advanced Energy Materials* **n/a**, 2402540.

58. Łopuszyński, M. & Majewski, J. A. Ordering in ternary nitride semiconducting alloys. *Phys. Rev. B* **85**, 035211 (2012).

59. Zhuk, S. *et al.* Synthesis and Characterization of the Ternary Nitride Semiconductor Zn_2VN_3: Theoretical Prediction, Combinatorial Screening, and Epitaxial Stabilization. *Chem. Mater.* **33**, 9306–9316 (2021).

60. Christian, T. M. *et al.* Amber-green light-emitting diodes using order-disorder $Al_xIn_{1-x}P$ heterostructures. *Journal of Applied Physics* **114**, 074505 (2013).

61. Greenaway, A. L. *et al.* Ternary Nitride Materials: Fundamentals and Emerging Device Applications. *Annual Review of Materials Research* **51**, 591–618 (2021).

62. Geoghegan, B. L. *et al.* Combining Valence-to-Core X-ray Emission and Cu K-edge X-ray Absorption Spectroscopies to Experimentally Assess Oxidation State in Organometallic Cu(I)/(II)/(III) Complexes. *J. Am. Chem. Soc.* **144**, 2520–2534 (2022).

63. Wang, J. *et al.* In situ X-ray spectroscopies beyond conventional X-ray absorption spectroscopy on deciphering dynamic configuration of electrocatalysts. *Nat Commun* **14**, 6576 (2023).

64. Kau, L. S., Spira-Solomon, D. J., Penner-Hahn, J. E., Hodgson, K. O. & Solomon, E. I. X-ray absorption edge determination of the oxidation state and coordination number of copper. Application to the type 3 site in Rhus vernicifera laccase and its reaction with oxygen. *J. Am. Chem. Soc.* **109**, 6433–6442 (1987).

65. Chaboy, J., Muñoz-Páez, A., Carrera, F., Merkling, P. & Marcos, E. S. *Ab initio* x-ray absorption study of copper K -edge XANES spectra in Cu(II) compounds. *Phys. Rev. B* **71**, 134208 (2005).

66. Beale, A. M., Gao, F., Lezcano-Gonzalez, I., Peden, C. H. F. & Szanyi, J. Recent advances in automotive catalysis for NO_x emission control by small-pore microporous materials. *Chem. Soc. Rev.* **44**, 7371–7405 (2015).

67. Bates, S. A. *et al.* Identification of the active Cu site in standard selective catalytic reduction with ammonia on Cu-SSZ-13. *Journal of Catalysis* **312**, 87–97 (2014).

68. Rehr, J. J., Kas, J. J., Vila, F. D., Prange, M. P. & Jorissen, K. Parameter-free calculations of X-ray spectra with FEFF9. *Phys. Chem. Chem. Phys.* **12**, 5503–5513 (2010).

69. Becker, S., Behrens, U. & Schindler, S. Synthesis, Structure and Reactivity of the Compound [Cu(C7H7NH2)Cl]4 derived from CuCl and Benzylamine (C7H7NH2). *Zeitschrift für anorganische und allgemeine Chemie* **641**, 430–435 (2015).

70. Yin, X. *et al.* Dish-like higher-ordered palladium nanostructures through metal ion-ligand complexation. *Nano Res.* **11**, 3442–3452 (2018).

71. Anantharaj, S. *et al.* Recent Trends and Perspectives in Electrochemical Water Splitting with an Emphasis on Sulfide, Selenide, and Phosphide Catalysts of Fe, Co, and Ni: A Review. *ACS Catal.* **6**, 8069–8097 (2016).

72. Shinagawa, T., Garcia-Esparza, A. T. & Takanabe, K. Insight on Tafel slopes from a microkinetic analysis of aqueous electrocatalysis for energy conversion. *Sci Rep* **5**, 13801 (2015).

73. Ma, Z., Li, Z., Li, S., Li, P. & Zhang, H. Nanostructured Ni2N thin films magnetron-sputtered on nickel foam as efficient electrocatalyst for hydrogen evolution reaction. *Materials Letters* **229**, 148–151 (2018).

74. Wang, W. *et al.* In-situ synthesis of coupled molybdenum carbide and molybdenum nitride as electrocatalyst for hydrogen evolution reaction. *Journal of Alloys and Compounds* **792**, 230–239 (2019).

75. Cheng, R. *et al.* Shrunken hollow Mo-N/Mo-C nanosphere structure for efficient hydrogen evolution in a broad pH range. *Electrochimica Acta* **298**, 799–805 (2019).

76. Yan, H. *et al.* Holey Reduced Graphene Oxide Coupled with an Mo_2N–Mo_2C Heterojunction for Efficient Hydrogen Evolution. *Advanced Materials* **30**, 1704156 (2018).

77. Cao, B., Veith, G. M., Neuefeind, J. C., Adzic, R. R. & Khalifah, P. G. Mixed Close-Packed Cobalt Molybdenum Nitrides as Non-noble Metal Electrocatalysts for the Hydrogen Evolution Reaction. *J. Am. Chem. Soc.* **135**, 19186–19192 (2013).

78. Wang, Y. *et al.* Porous cobalt-iron nitride nanowires as excellent bifunctional electrocatalysts for overall water splitting. *Chemical Communications* **52**, 12614–12617 (2016).

79. Hu, H. *et al.* Intrinsic Properties of Macroscopically Tuned Gallium Nitride Single-Crystalline Facets for Electrocatalytic Hydrogen Evolution. *Chemistry – A European Journal* **25**, 10420–10426 (2019).

80. Ma, L., Ting, L. R. L., Molinari, V., Giordano, C. & Yeo, B. S. Efficient hydrogen evolution reaction catalyzed by molybdenum carbide and molybdenum nitride nanocatalysts synthesized via the urea glass route. *J. Mater. Chem. A* **3**, 8361–8368 (2015).

81. Song, Y.-J. & Yuan, Z.-Y. One-pot Synthesis of Mo_2N/NC Catalysts with Enhanced Electrocatalytic Activity for Hydrogen Evolution Reaction. *Electrochimica Acta* **246**, 536–543 (2017).

82. Chen, Q. *et al.* Bifunctional Iron–Nickel Nitride Nanoparticles as Flexible and Robust Electrode for Overall Water Splitting. *Electrochimica Acta* **247**, 666–673 (2017).

83. Jia, X. *et al.* Ni_3FeN Nanoparticles Derived from Ultrathin NiFe-Layered Double Hydroxide Nanosheets: An Efficient Overall Water Splitting Electrocatalyst. *Advanced Energy Materials* **6**, 1502585 (2016).

84. Xie, L. *et al.* In situ formation of a 3D core/shell structured Ni_3N@Ni–Bi nanosheet array: an efficient non-noble-metal bifunctional electrocatalyst toward full water splitting under near-neutral conditions. *J. Mater. Chem. A* **5**, 7806–7810 (2017).

85. Wang, C. *et al.* Easy access to trace-loading of Pt on inert Ni_3N nanoparticles with significantly improved hydrogen evolution activity at entire pH values. *Electrochimica Acta* **320**, 134597 (2019).

86. Han, L., Feng, K. & Chen, Z. Self-Supported Cobalt Nickel Nitride Nanowires Electrode for Overall Electrochemical Water Splitting. *Energy Technology* **5**, 1908–1911 (2017).

87. Lai, J., Huang, B., Chao, Y., Chen, X. & Guo, S. Strongly Coupled Nickel–Cobalt Nitrides/Carbon Hybrid Nanocages with Pt-Like Activity for Hydrogen Evolution Catalysis. *Advanced Materials* **31**, 1805541 (2019).

88. Shanker, G. S., Markad, G. B., Jagadeeswararao, M., Bansode, U. & Nag, A. Colloidal Nanocomposite of TiN and N-Doped Few-Layer Graphene for Plasmonics and Electrocatalysis. *ACS Energy Lett.* **2**, 2251–2256 (2017).

89. Wang, C. *et al.* Quasi-atomic-scale platinum anchored on porous titanium nitride nanorod arrays for highly efficient hydrogen evolution. *Electrochimica Acta* **292**, 727–735 (2018).

90. Zhang, N. *et al.* Co,N-Codoped porous vanadium nitride nanoplates as superior bifunctional Cite this: Nanoscale, 2019, 11, 11542 electrocatalysts for hydrogen evolution and oxygen reduction reactions. (2019).

91. Wei, B. *et al.* Bimetallic vanadium-molybdenum nitrides using magnetron co-sputtering as alkaline hydrogen evolution catalyst. *Electrochemistry Communications* **93**, 166–170 (2018).

92. Yang, H. *et al.* Efficient hydrogen and oxygen evolution electrocatalysis by cobalt and phosphorus dual-doped vanadium nitride nanowires. *Materials Today Chemistry* **11**, 1–7 (2019).

93. Zhao, Y., Kamiya, K., Hashimoto, K. & Nakanishi, S. Hydrogen Evolution by Tungsten Carbonitride Nanoelectrocatalysts Synthesized by the Formation of a Tungsten Acid/Polymer Hybrid In Situ. *Angewandte Chemie International Edition* **52**, 13638–13641 (2013).

94. Shi, J. *et al.* Tungsten nitride nanorods array grown on carbon cloth as an efficient hydrogen evolution cathode at all pH values. *Electrochimica Acta* **154**, 345–351 (2015).

95. Song, F. *et al.* Interfacial Sites between Cobalt Nitride and Cobalt Act as Bifunctional Catalysts for Hydrogen Electrochemistry. *ACS Energy Lett.* **4**, 1594–1601 (2019).

96. Gauthier, C., Solé, V. A., Signorato, R., Goulon, J. & Moguiline, E. The ESRF beamline ID26: X-ray absorption on ultra dilute sample. *J Synchrotron Radiat* **6**, 164–166 (1999).

97. Glatzel, P. *et al.* The five-analyzer point-to-point scanning crystal spectrometer at ESRF ID26. *J Synchrotron Rad* **28**, 362–371 (2021).

98. Caliebe, W. A., Murzin, V., Kalinko, A. & Görlitz, M. High-flux XAFS-beamline P64 at PETRA III. in 060031 (Taipei, Taiwan, 2019). doi:10.1063/1.5084662.

99. Pascarelli, S. *et al.* The Time-resolved and Extreme-conditions XAS (TEXAS) facility at the European Synchrotron Radiation Facility: the energy-dispersive X-ray absorption spectroscopy beamline ID24. *J Synchrotron Radiat* **23**, 353–368 (2016).

100. Zhang, H. *et al.* Bifunctional Heterostructure Assembly of NiFe LDH Nanosheets on NiCoP Nanowires for Highly Efficient and Stable Overall Water Splitting. *Advanced Functional Materials* **28**, 1706847 (2018).

101. Toby, B. H. & Von Dreele, R. B. GSAS-II: the genesis of a modern open-source all purpose crystallography software package. *J Appl Cryst* **46**, 544–549 (2013).